NeuroImage 193 (2019) 126–138

Contents lists available at ScienceDirect

NeuroImage

journal homepage: www.elsevier.com/locate/neuroimage

Integrated radiofrequency array and animal holder design for minimizing head motion during awake marmoset functional magnetic resonance imaging

David J. Schaeffer [a,1], Kyle M. Gilbert [a,1], Yuki Hori [a], Joseph S. Gati [a], Ravi S. Menon [a,b], Stefan Everling [a,b,*]

[a] Centre for Functional and Metabolic Mapping, Robarts Research Institute, University of Western Ontario, London, Ontario, Canada
[b] Department of Physiology and Pharmacology, University of Western Ontario, London, Ontario, Canada

ARTICLE INFO

Keywords:
Common marmoset
Resting state functional magnetic resonance imaging
Receive coil
Animal holder
CAD (computer-aided design)

ABSTRACT

Marmosets are small New World primates that are posited to become an important preclinical animal model for studying intractable human brain diseases. A critical step in the development of marmosets as a viable model for human brain dysfunction is to characterize brain networks that are homologous with human network topologies. In this regard, the use of functional magnetic resonance imaging (fMRI) holds tremendous potential for functional brain mapping in marmosets. Although possible, implementation of hardware for fMRI in awake marmosets (free of the confounding effects of anesthesia) is not trivial due to the technical challenges associated with developing specialized imaging hardware. Here, we describe the design and implementation of a marmoset holder and head-fixation system with an integrated receive coil for awake marmoset fMRI. This design minimized head motion, with less than 100 μm of translation and 0.5 degrees of rotation over 15 consecutive resting state fMRI runs (at 15 min each) across 3 different marmosets. The fMRI data was of sufficient quality to reliably extract 8 resting state networks from each animal with only 60–90 min of resting state fMRI acquisition per animal. The restraint system proved to be an efficient and practical solution for securing an awake marmoset and positioning a receive array within minutes, limiting stress to the animal. This design is also amenable for multimodal imaging, allowing for electrode or lens placement above the skull via the open chamber design. All computer-aided-design (CAD) files and engineering drawings are provided as an open resource, with the majority of the parts designed to be 3D printed.

1. Introduction

Marmosets are small New World primates with a mostly smooth (lissencephalic) cortex, offering unique possibilities for studying mechanistic neuron-type and layer-specific circuits supporting primate-specific higher cognitive and sensori-motoric functions not possible in other primate species (Walker et al., 2017). Marmosets are also posited to become an important preclinical animal model for studying intractable human brain diseases, offering advantages over both rodents and Old World non-human primate models. Marmosets, unlike rodents, have a granular dorsolateral prefrontal cortex (Preuss, 1995), a brain area frequently linked to neuropsychiatric disorders (Goldman-Rakic, 1999). As such, while not much larger than a rat (at ~350 g), the marmoset possesses a brain that parallels the human brain more closely than does the rodent brain. Their small size is advantageous over other larger non-human primate models (e.g., macaques), as it is possible to image the marmoset brain using ultra-high field small-bore magnetic resonance imaging (MRI) scanners typically employed for rodent studies (often allowing for superior signal-to-noise ratio and resolution). Although possible, the implementation of small-bore marmoset MRI is not trivial due to the technical challenges associated with developing specialized imaging hardware (Papoti et al., 2013, 2014, 2017; Gilbert et al., 2017, 2019) – commercially available radiofrequency coils designed for rodents are often not optimized for the significantly larger marmoset head and brain, especially for accelerated echo-planar imaging sequences requiring multi-channel receive arrays (e.g., functional MRI (fMRI),

* Corresponding author. Robarts Research Institute, University of Western Ontario, London, Ontario, Canada.
E-mail address: severlin@uwo.ca (S. Everling).
[1] Authors contributed equally to this work.

https://doi.org/10.1016/j.neuroimage.2019.03.023
Received 16 January 2019; Received in revised form 1 March 2019; Accepted 11 March 2019
Available online 15 March 2019
1053-8119/© 2019 Elsevier Inc. All rights reserved.

diffusion tensor imaging, arterial spin labelling). Here, we offer open-source hardware designs for an integrated radiofrequency coil and animal holder that allows for stable head-fixation (via a surgically implanted chamber) and high-quality functional imaging (e.g., high temporal signal-to-noise (SNR) ratio, reliable resting state network maps) of awake marmosets at ultra-high field.

A critical step in the development of marmosets as a viable model for human brain dysfunction is to characterize brain networks that are homologous with human network topologies. Although tracing studies have started to provide detailed knowledge of marmoset brain connectivity (see Majka et al., 2016 for atlas) these studies do not provide information about functional interactions amongst regions across the brain. In this regard, the use of fMRI holds tremendous potential for functional brain mapping in marmosets. Indeed, our lab has employed anesthetized resting-state fMRI to demonstrate homologies in functional network topologies across marmosets, macaques, and humans (Ghahremani et al., 2017; Schaeffer et al., 2019a, 2019b). There are some caveats to imaging under anesthesia, however, with mounting evidence to suggest that anesthesia obfuscates the true connectivity profiles of the resting brain (Liu et al., 2013; Hutchison et al., 2014). Mapping these circuitries in fully awake marmosets, therefore, is invaluable for accurately mapping homologous brain circuitries in healthy and altered states (e.g., by way of optogenetic or pharmacological manipulation). Perhaps more importantly, awake marmoset imaging allows for the use of behavioral paradigms during functional imaging (i.e., task-based fMRI), allowing for identification of the circuities underlying marmoset behavior (and the manipulation thereof).

In recent years, clever hardware designs (Meyer et al., 2006; Papoti et al., 2013, 2014, 2017) have allowed for awake marmoset fMRI, and major in-roads have been made into mapping awake marmoset circuitry (Belcher et al., 2013, 2016; Liu et al., 2013; Hung et al., 2015b, 2015a; Silva, 2017; Toarmino et al., 2017; Hirano et al., 2018; Yen et al., 2018). The majority of these published studies, however, utilize custom-designed helmet coils (as described in Papoti et al., 2013; Silva et al., 2011) – this system is well conceived and ideal for truly non-invasive imaging, but requires a custom helmet to be built for each animal. Here, we present a more universal system, making use of a surgically implanted head chamber that allows for awake fMRI in stereotactic position while also being compatible (in principle) with simultaneous electrophysiological recoding in the MRI scanner. This same implanted head chamber is also compatible with existing published designs for upright behavioral training and electrophysiological recordings in a stereotactic frame (Johnston et al., 2018, 2019). To demonstrate the utility of the design, we present quality assessments from the coil (coil coupling, noise correlations, and SNR), estimates of head motion, and resting state data (independent component analysis (ICA) extracted resting state networks) from three marmosets. We have made all of the computer-aided-design files publicly available (https://web.gin.g-node.org/everling_lab_marmosets). The majority of the components (aside from the electronics and nylon hardware) can be three-dimensionally (3D) printed using MRI-compatible material at very low cost.

2. Methods

2.1. Subjects

All surgical, training, and imaging procedures described below were carried out on three male common marmosets (*Callithrix jacchus*), weighing 380 g (Marmoset Bi), 245 g (Marmoset Ba), and 305 g (Marmoset Mi). Marmosets were 3, 1.5, and 1.5 years old, respectively, at the time of the experiments. Experimental procedures were in accordance with the Canadian Council of Animal Care policy and a protocol approved by the Animal Care Committee of the University of Western Ontario Council on Animal Care.

2.2. Surgical implantation

All three marmosets underwent an aseptic surgical procedure to implant a head chamber while the animal was placed in a stereotactic frame (Narishige, Model SR-6C-HT). The surgical procedure was identical to that described in Johnston et al. (2018), apart from the type of adhesive used to attach the chamber to the skull and the material used to build the chamber – different materials were required to avoid large magnetic susceptibility differences between the chamber, adhesive, and the surrounding tissue, which can cause signal loss in T_2*-weighted fMRI. Specifically, several coats of adhesive resin (All-bond Universal, Bisco, Schaumburg, Illinois, USA) were applied using a microbrush, air dried, and cured with an ultraviolet dental curing light (King Dental). Then, a two-component dental cement (C & B Cement, Bisco, Schaumburg, Illinois, USA) was applied to the skull and to the bottom of the chamber, which was then lowered onto the skull via a stereotactic manipulator to ensure correct location and orientation. Through the course of numerous surgeries prior to this study, we have found that the initial coating of the adhesive resin greatly improves holding power, likely due to improved biocompatibility (i.e., adhesion of the cement to the resin, rather than to the skull directly). Here, the chamber was 3D printed at 0.25 mm resolution using stereolithography and a clear photopolymer resin (Clear Resin V4; Form 2, Formlabs, Somerville, Massachusetts, USA) – this chamber is also commercially available in machined polyether ether keton (PEEK; Neuronitek, London, Ontario, Canada). The printed chamber was then washed in 99% isopropyl alcohol (8600-1-40; Caledon Laboratories Limited, Georgetown, ON, Canada) and cured with ultraviolet light (Form Wash and Form Cure; Formlabs, Somerville, Massachusetts, USA). Given that this material does not withstand the heat of an autoclave, the chambers were soaked in disinfectant (Metricide, Metrex, Orange, California, USA) until the chamber was ready to be implanted. A removable PEEK cap (Neuronitek, London, Ontario, Canada) was attached to the chamber via set screws – this cap was removed prior to entry into the MRI.

2.3. Hardware design

2.3.1. Animal holder

All hardware was designed in concert with veterinary technicians to minimize animal discomfort and improve handling efficiency. The base of the design was a 7 cm inner-diameter acrylic tube (8532K23; McMASTER-CARR, Aurora, Ohio, USA) in which a ~400 g marmoset could comfortably lie in the sphinx position. The animal holder was designed to first allow the animals to become acclimatized to the tube-design while they were restrained with neck and tail plates (Fig. 1), then for quick and efficient head-fixation through the use of hinged fixation pin assemblies and a retractable clamp (via two elastic O-rings). At the front of the assembly is a modular attachment that can be switched between a camera (Model 12M-i, MRC Systems GmbH, Heidelberg, Germany) and reward tube assembly (for awake behavior) or a separate assembly with a mask for anesthetic delivery (i.e., for anesthetized comparisons, or excessively long anatomical imaging). Aside from the electronics and nylon hardware, all parts were 3D printed at 0.25 mm resolution using stereolithography and a clear photopolymer resin (Clear Resin V4; Form 2, Formlabs, Somerville, Massachusetts, USA). We opted for a machined acrylic tube for durability and cost, but this component can also be 3D printed.

2.3.2. Receive array

The receive array (Fig. 2) was comprised of five loops integrated into the interior of the coil former. When tightening the screw to secure the chamber, two conducting posts (6–32 brass screws) on one clamp push into two conductive pads on the opposite clamp to electrically connect the element circumscribing the chamber. Conductive pads consisted of copper braid wrapped around 4-mm-thick ethylene-vinyl-acetate (EVA)

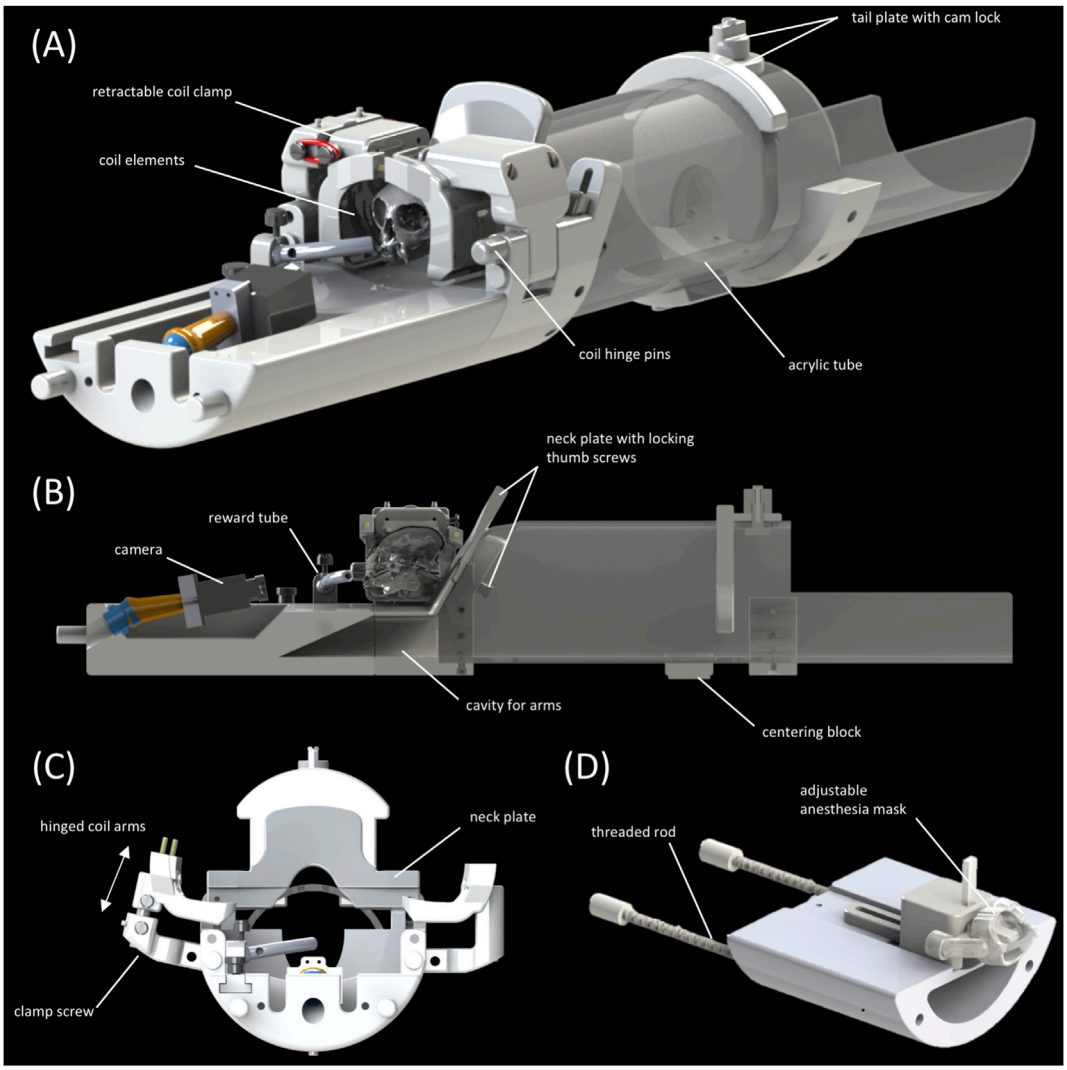

Fig. 1. Rendered CAD drawings of the animal holder and radiofrequency coil former. (A) shows a marmoset skull rendering (for display only) fixed in position via the retractable coil hinges and clamp. (B) shows a cross-sectional view, demonstrating the cavity for the arms, along with the adjustable reward tube and camera. The angle of the neck plate and receive coil is required to accommodate the marmoset's body. (C) shows the opening of the neck and tail plates along with the hinging of the coil arms. When the coil arms are fully opened, the marmoset is not able to reach the coil formers, allowing for restraint by the neck and tail plates prior to head-fixation; this also allows for training without head-fixation. To fix the animal, the coil arms are closed and locked in place by inserting the hinge pins. The retractable clamp is then used to tighten the fixation pins against the chamber by turning a flat-head screw. (D) shows the optional marmoset-specific anesthesia mask for anesthetized imaging (e.g., prior to animal acclimatization).

foam and soldered to the opposing half of the coil loop. The elasticity of the foam ensured a firm contact between the conducting post and the pad; no spiking artifacts were therefore visible during imaging. By creating a coil element around the chamber, whole-brain receive sensitivity was achieved despite the geometrical limitations imposed by the chamber.

The size and location of the chamber allowed for only one coil element to be placed at the superior aspect of the head. Two coil elements, distributed in the anterior-posterior direction, were located on either side of the head, for a total of five elements. This allowed for a modest acceleration rate (two-fold) in the anterior-posterior or left-right directions during parallel imaging. All coil elements were geometrically overlapped to reduce inter-element coil coupling (Roemer et al., 1990).

Coil elements were constructed from 22-AWG insulated copper wire adhered to the inner surface of the receive former for close proximity to the skull and brain. Each element included three to five distributed capacitors (American Technical Ceramics, 100B series) to reduce conservative electric fields from interacting with the head (which was in close proximity) – this included variable capacitors (Sprague-Goodman Electronics, SGC3 series) for tuning and matching. Circuit boards were mounted on the exterior of the former. These boards were comprised of a parallel matching capacitor, a tuning capacitor, an active-detuning circuit, a serial capacitor for fine-tuning preamplifier decoupling, and a choke balun. Circuit boards were connected to low-input-impedance preamplifiers (Stark Contrast, Erlangen, Germany) with RG178 coaxial cables (41–54 cm long) and non-magnetic MCX connectors: the cables transformed the input impedance of the preamplifier to a parallel-resonant inductance across the matching capacitor, thereby reducing inter-element coupling (Roemer et al., 1990). Preamplifiers were located posterior to the animal to prevent obstructions to the animal's line-of-sight. The resultant loss of the 54-cm-long cable and MCX connectors was 0.54 dB (equating to less than a 6% reduction in SNR). All coil elements were tuned to 400.2 MHz and matched to 50 Ohms (the optimal impedance to minimize the preamplifier's noise figure) when loaded with a 50-mm NaCl spherical phantom approximating the size of an adult marmoset head.

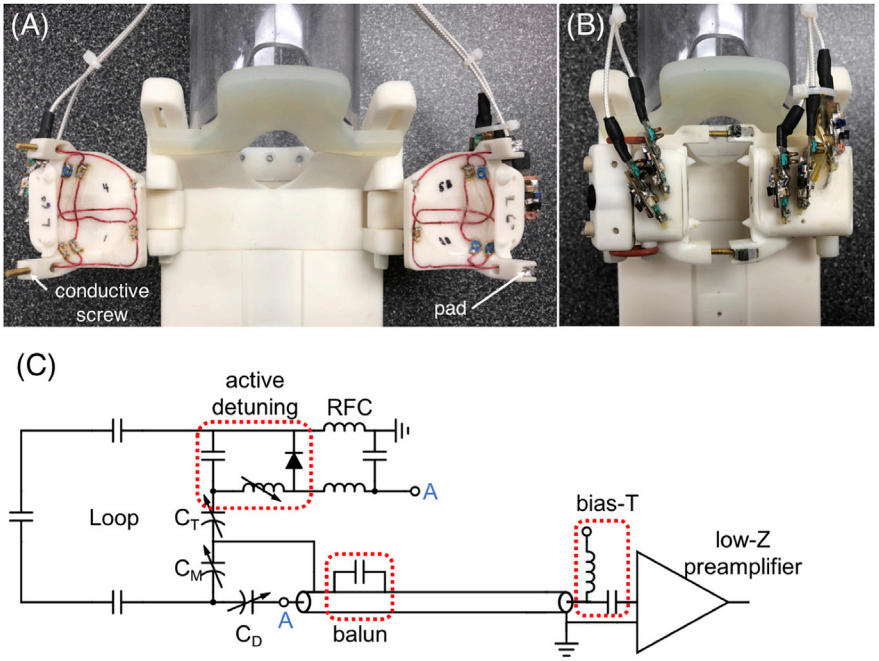

Fig. 2. A photograph of the marmoset coil when (A) open and (B) closed. Two brass screws are pressed into opposing conductive pads (tinned copper braid wrapped on EVA foam) to electrically complete the loop encircling the chamber. The tightening screw (see Fig. 1) ensures a solid connection to the pads to decrease coil noise and prevent spiking artifacts. Panel (B) shows circuits for matching, active detuning, and balancing are located on circuit boards mounted to the top of the coil former. Low-input-impedance preamplifiers are located behind the animal, so as not to obstruct the view of the animal. Panel (C) shows a circuit schematic of a single receive element. The circuit board was double-sided with an electrical connection between points denoted by 'A': this allowed direct current injected into the bias-T to bias the PIN diode in the active-detuning circuit. RFC: radiofrequency choke; C_M: matching capacitor; C_T: tuning capacitor; C_D: preamplifier-decoupling capacitor.

2.4. Animal training and fixation procedure

All animals were first acclimatized to the animal holder, head-fixation system, and a mock MRI environment prior to the first imaging session (procedure adapted from that described in Silva et al., 2011). Each marmoset was trained over the course of three weeks. During the first week, marmosets entered the tube and were constrained using only the neck and tail plates (see Fig. 1), for increasingly long durations (up to 30 min). During the second week, the restraint tube was inserted into a mock MRI tube (a 12 cm inner diameter tube) to simulate the scanner environment; MRI sounds were played at increasingly loud volumes (up to ~80 dB) and for increasing long durations, up to 60 min sessions. In week 3, marmosets were head-fixed via the fixation pins, inserted into the mock MRI tube and exposed to MRI sounds. Within each session, the animals were presented with reward items (pudding or marshmallow fluff) for remaining still (calmly facing forward, with minimal movement of limbs). Throughout the training sessions, the behavioral rating scale described by Silva et al. (2011) was used to assess the animals' tolerance to the acclimatization procedure – by the end of week 3, all three marmosets scored 1 or 2 on this assessment scale (see Silva et al., 2011, Table 2) showing calm and quiet behavior, with little sign of agitation. After this time, each marmoset participated in an MRI session during which awake resting state MRI was collected. Typically, it took less than 10 min to remove the animal from the transfer case, restrain and head-fix the animal, and start the first imaging sequence. To minimize the time in which the animals were head-fixed, we closed the fixation pins in the scanner room (with an MR compatible screw driver). Once fixed, a gel (see *Image Distortion* section below) was quickly squeezed into the chamber and applied to the brow ridge (using a cotton swab) to reduce magnetic susceptibility artifacts. During imaging sessions, marmosets were continuously monitored by a veterinary technician for any sign of struggle or discomfort via an MR compatible camera.

2.5. Image acquisition

Data were acquired using a 9.4 T 31 cm horizontal bore magnet (Varian/Agilent, Yarnton, UK) and Bruker BioSpec Avance III console with the software package Paravision-6 (Bruker BioSpin Corp, Billerica, MA), a custom-built high-performance 15-cm-diameter gradient coil with 400-mT/m maximum gradient strength (xMR, London, CAN; Peterson et al., 2018), and the receive coil described above. Radio-frequency transmission was accomplished with a quadrature birdcage coil (12-cm inner diameter) built in-house. All imaging was performed at the Centre for Functional and Metabolic Mapping at the University of Western Ontario.

Functional imaging was performed over multiple sessions (days) for each animal, with 4–6 functional runs (at 600 vol each) per animal with the following parameters: TR = 1500 ms, TE = 15 ms, flip angle = 35°, field of view = 64 × 64 mm, matrix size = 128 × 128, voxel size = 0.5 × 0.5 × 0.5 mm, slices = 42, bandwidth = 500 kHz, GRAPPA acceleration factor: 2 (anterior-posterior). All functional images were acquired in the axial orientation. Prior to functional image acquisition, B_0 shimming was performed after the collection of a B_0 field map of the entire marmoset brain produced from a dual-echo gradient echo acquisition. A 3D-ellipsoid adjustment volume was used as a target for shim calculations whereby linear (X, Y, Z), second (Z^2, XY, XZ, YZ, X^2-Y^2) and third (Z^3, X^3, Y^3, ZXY, ZX^2-ZY^2) order shims were applied using a constrained minimization approach. T2-weighted structural scans were acquired for each animal during one of the awake sessions with the following parameters: TR = 5500 ms, TE = 53 ms, field of view = 51.2 × 51.2 mm, matrix size = 384 × 384, voxel size = 0.133 × 0.133 × 0.5 mm, slices = 42, bandwidth = 50 kHz, GRAPPA acceleration factor: 2.

2.6. Coil evaluation

Geometric decoupling (S_{12}), preamplifier decoupling, and active detuning were measured using standard techniques (Keil et al., 2011). To assess the cumulative effectiveness of inter-element decoupling, an *in vivo* noise correlation matrix was calculated from the complex data of a noise-only acquisition.

The spatial sensitivity of the receive coil was evaluated by acquiring maps of spatial SNR (3D FLASH; orientation: axial, resolution: 400-μm isotropic, FOV: 48 × 48 × 48 mm, TE/TR: 5/12 ms, bandwidth: 20 kHz, flip angle: 10°, number of averages: 2, acquisition time: 6 min 40 s) in a fully awake marmoset. Spatial SNR was derived from acquisitions with and without RF transmission: the image from each receive element was divided by the standard deviation of the corresponding (complex) noise-only image. The sum-of-squares combined SNR map was calculated in an analogous fashion. All calculations were performed in Matlab (The MathWorks, Natick, MA).

2.7. Image analysis

2.7.1. Image distortion

Given that skull-attached chambers are generally accompanied by magnetic-susceptibility image artifacts (via differences in the magnetic susceptibility between the chamber, adhesive, air, and tissue, as well as the surgical displacement of the skin, fat, and muscle), we sought to ameliorate this distortion by filling the chamber with a water-based lubricant gel (MUKO SM321N, Canadian Custom Packaging Company, Toronto, Ontario, Canada). A similar method has been applied to mouse imaging at ultra-high field by molding agarose around the head (Adamczak et al., 2010) – this method works by moving large susceptibility mismatches away from the brain, thereby improving B_0 homogeneity in the brain and thus decreasing geometric distortion. Functional images were acquired on monkey Bi with an empty head chamber, then again with the chamber filled with the gel (and also applied to the brow ridge) to evaluate the reduction in image distortion (via temporal SNR maps). Although other easily removable liquids could be used to fill the camber, the viscous gel allows for application to the brow ridge without dripping into the eyes. Generally, we found that a thin film (of approximately 2–3 mm) of the lubricant gel on the brow ridge was sufficient to ameliorate the associated geometric distortion.

2.7.2. Motion evaluation

For each animal, head motion was estimated by registering each functional volume to the middle volume of that run using AFNI's (Cox, 1996) 3dvolreg program – six motion parameters (x, y, z translation and rotation) were extracted for each functional run. A systematic linear trend of apparent posterior movement (~0.15 mm of total translation) was observed in every imaging run: to verify that this trend was scanner related (i.e., thermal frequency drift due to gradient heating), rather than animal related, we repeated the functional sequence on an agar phantom using multiple phase encoding directions.

2.7.3. Image preprocessing

Data was preprocessed using AFNI (Cox, 1996) and FSL software (Smith et al., 2004). Raw functional images were converted to Neuro Informatics Technology Initiative (NifTI) format using dcm2niix (Li et al., 2016) and reoriented from the sphinx position using FSL. The images were then volume registered to the middle volume (AFNI's 3dvolreg). An average functional image was then calculated for each session and registered (FSL's FLIRT) to each animal's T2-weighted image, then the 4D time series was registered to T2 space using this transformation matrix. T2-weighted images were manually skull-stripped, and this mask was applied to the functional images.

T2-weighted images were non-linearly registered to the NIH marmoset brain atlas (Liu et al., 2018) using FSL's FNIRT, and the resultant transformation matrices were later applied to the functional images (see below). The olfactory bulb was manually removed from the T2-weighted images of each animal prior to registration, as it was not included in the template image.

2.7.4. Resting state network analysis

Principal component analysis (PCA) was applied to remove the unstructured noise from each animal's time course using FSL's Multivariate Exploratory Linear Optimized Decomposition into Independent Components (MELODIC) software, followed by independent component analysis (ICA) with 50 dimensions. The resultant components were classified as signal or noise based on the criteria as shown in previous reports (Griffanti et al., 2017). Noise components were regressed from each fMRI time course using FSL's fsl_regfilt software. Using these fMRI data, ICA with 20 dimensions was re-performed for each subject to detect the neural components. The components (still in T2 native space for each animal) were finally normalized to the NIH template using T2-to-template transformation matrix described above.

3. Results

3.1. Coil evaluation

The mean and maximum S_{12} between receive elements was −18 dB and −12 dB, respectively. Preamplifier decoupling added a further 10–13 dB of isolation, resulting in a mean and maximum *in vivo* noise correlation of 19% and 38%, respectively. These noise correlation values are respectable given the range in coil size required to accommodate the chamber. Active detuning provided a mean isolation of −32 dB between receive elements and the transmit coil during transmission, ensuring the fidelity of the transmit field.

The mean spatial SNR over the brain of individual receive channels differed by only 23%, while the range in noise level between receive channels was likewise small (11%). This indicates similar sensitivity and noise characteristics between coil elements. Spatial SNR maps (Fig. 3) demonstrate the whole-brain coverage of the receive coil and can be used to compare this design to existing marmoset coil designs. Receive sensitivity profiles of the individual elements are proportional to the spatial SNR profiles.

Although the chamber placed restrictions on the geometry of the receive coil, five elements could still be placed around the head for whole-brain coverage, and modest acceleration rates were achievable. This allowed the echo train length to be reduced during functional imaging, thereby reducing image distortion at 9.4 T.

3.2. Image analysis

3.2.1. Image distortion

We sought to mitigate image distortion by filling the chamber with a water-based lubricant gel. Functional images were acquired on monkey Bi with an empty head chamber, then again with the chamber filled with the gel (and also applied to the brow ridge) to evaluate the reduction in image distortion (via temporal SNR maps). As shown in Fig. 4, the magnitude of temporal SNR in frontal cortex was dependent on the application of gel in the chamber and above the brow ridge.

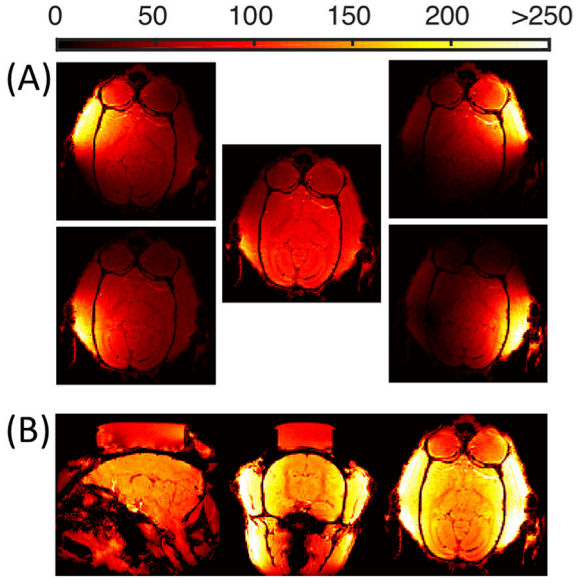

Fig. 3. (A) Spatial SNR profiles of the five individual receive coils. The central element is located at the superior aspect of the head, and therefore shows more uniform SNR in the axial slice orientation. (B) Sum-of-squares combined SNR maps show high SNR in the peripheral cortex. The gel (placed in and around the chamber) is visible at the superior aspect of the head.

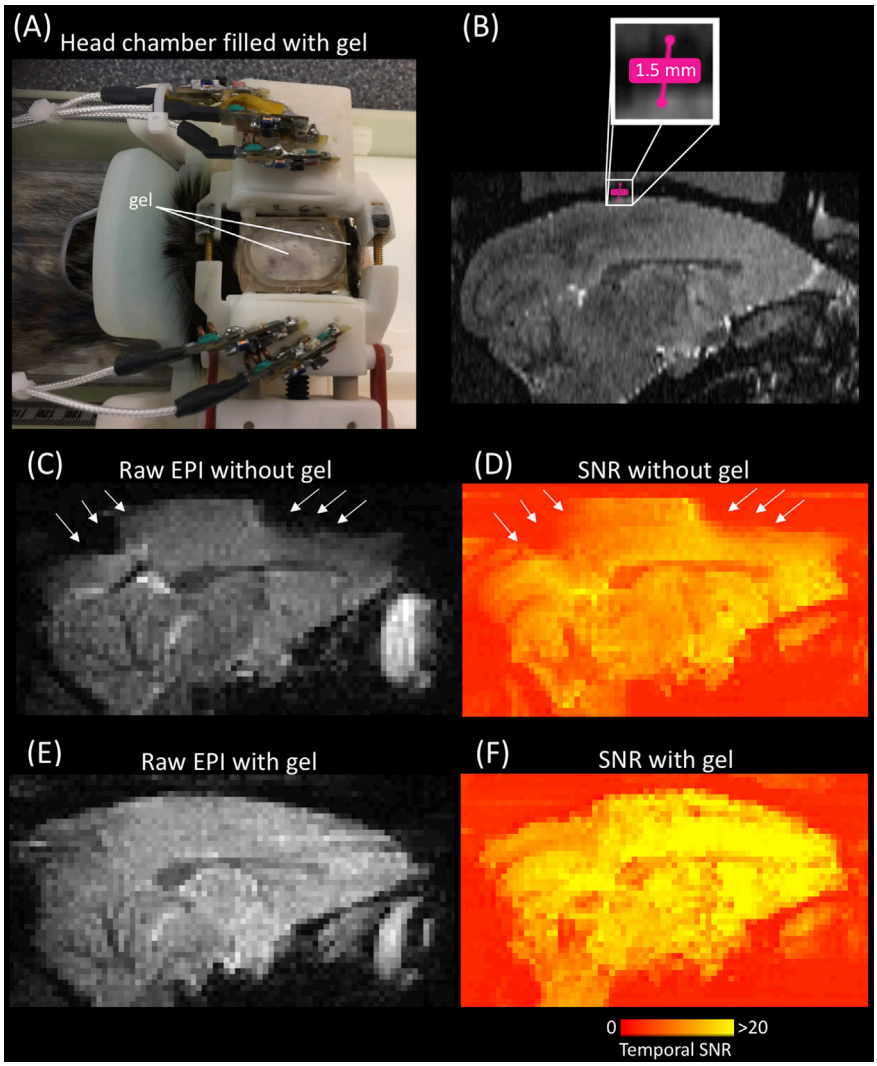

Fig. 4. Panel (A) shows a photograph of a marmoset fixed into position and the head chamber filled with gel to reduce geometric distortion. The gel was also applied to the brow ridge, allowing for a reduction in distortion in frontal cortex. Panel (B) shows a T2-weighted image of the brain and the chamber (and brow ridge) coated with gel. The white box is a zoomed view of the distance measurement between the top of the brain and the bottom of the gel, at only 1.5 mm – without the gel, this very small distance between the brain and open air results in image distortion (panels C (single volume EPI) and D (temporal SNR of 600 vol)). With the gel in the chamber, however, a high temporal SNR is achieved in the areas of previous signal loss (panels E (single volume EPI) & D (temporal SNR of 600 vol)). As such, the gel (or another similar medium) is necessary for high signal adjacent to the chamber.

3.2.2. *Motion evaluation*

For each animal, head motion was estimated by registering each functional volume to the middle volume of that run. The six extracted motion parameters (x, y, z translation and rotation) are shown in Fig. 5. A linear trend of posterior movement (~0.15 mm total translation) was present in all 15 runs across the three marmosets. However, when the functional sequence was repeated on a phantom using multiple phase encoding directions, this linear trend always coincided with the phase-encode direction; therefore, the anterior-to-posterior translation pattern across all 15 runs was most likely due to thermal frequency drift, and not due to animal motion. Maximal translation across all three runs, then, was less than 100 μm and rotation was less than 0.5° total in all of the animals; therefore, the chamber design was extremely stable.

3.2.3. *Resting state network analysis*

The results of the ICA resting state network analysis (z-score maps) are shown on surface maps (Liu et al., 2018) in Figs. 6 and 7 and volumetrically in Figs. 8 and 9. ICA analyses were conducted separately in each animal (via time course concatenation) using a 20 component limit. Eight common components were identified across all three animals, suggesting reliability of data quality. The following network components were consistent with known resting state networks (Belcher et al., 2013; Ghahremani et al., 2017): frontoparietal, somatomotor (dorsal), somatomotor (ventral), auditory, basal ganglia, primary visual, high-order visual (posterior), and high-order visual (anterior) networks were identified across all three animals. The frontoparietal network showed peaks along the intraparietal sulcus, posterior cingulate (23a, 23b, PGM, 19M, 23v), and dorsolateral prefrontal cortex (6DR, 8aD). The somatomotor (dorsal) network showed peaks in primary somatosensory areas (3a, 3b, and 1/2), primary motor areas (4 ab), and middle/posterior cingulate (24a-d, 23c, 31). The somatomotor (ventral) network showed peaks in primary somatosensory areas (3a, 3b, and 1/2) that extended anteriorly (6Va, 4c, 8c), with weaker connectivity to midcingulate than the somatomotor (dorsal) network. The auditory network showed peaks in auditory cortex (better visualized in subcortical Fig. 8, than on the surfaces in Fig. 6) and anterior cingulate (32, 24b, albeit some differences across animals). The basal ganglia network showed subcortical peaks in caudate and putamen and cortical peaks in midcingulate and lateral parietal cortex. The primary visual network showed peaks in V1, 19M, and areas MT and MST (although somewhat lateralized; see Fig. 9). The high-order visual (posterior) network showed peaks in visual areas (V2, V3, V4, 19DI, V4T, and V5; with Monkey Ba and Bi, showing more anterior peaks), intraparietal sulcus, and dorsolateral prefrontal cortex (8 aV). The high-order visual (anterior) network showed peaks that extended across lateral temporal cortices (see Fig. 7 for specific regions).

4. Discussion

Here, we present openly available designs for an integrated radio-frequency coil and animal holder that makes use of a surgically implanted

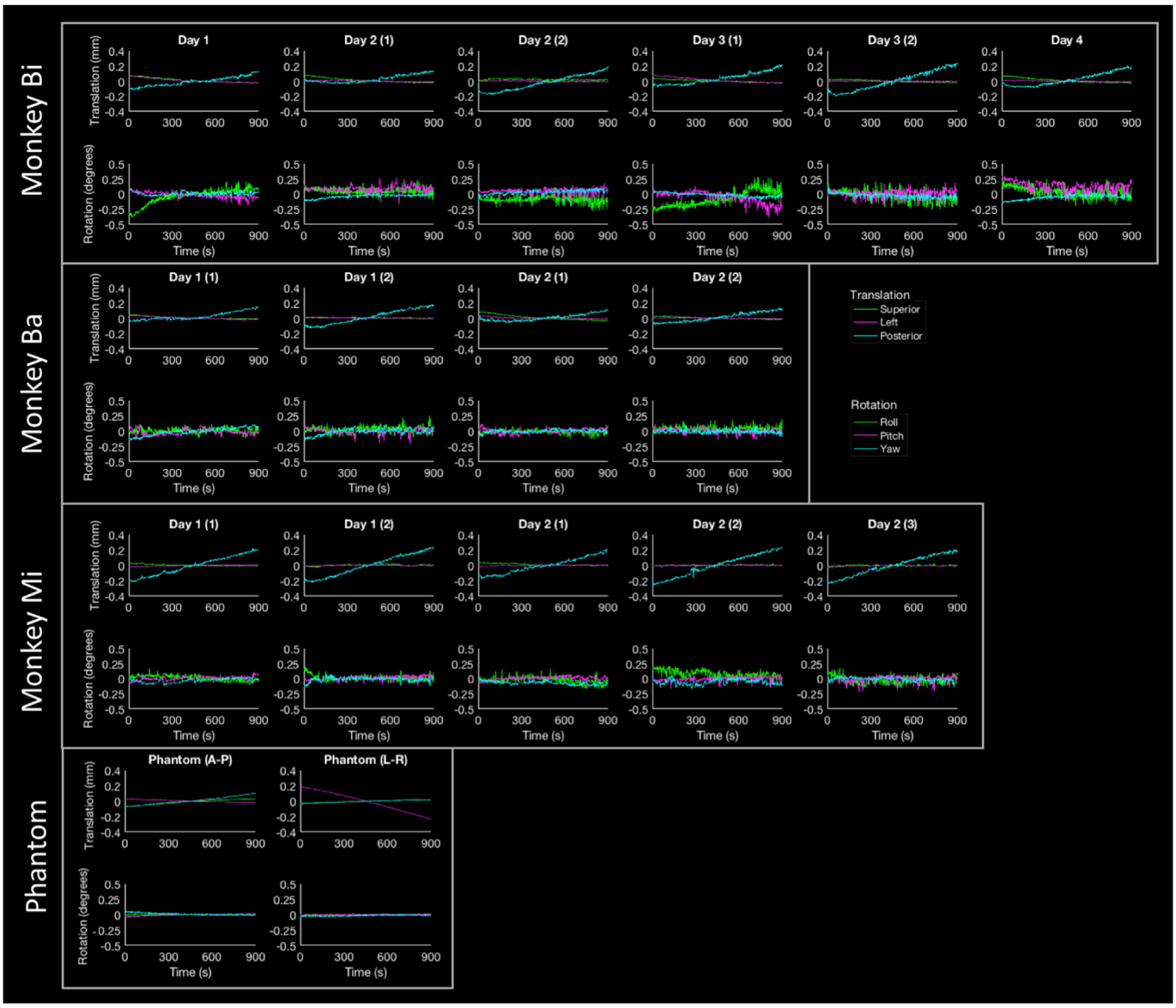

Fig. 5. Estimates of head motion for three marmosets and an agar phantom. The top panel shows translation (upper row) and rotation (lower row) estimates for monkey Bi, with each column showing a separate 600 vol resting state fMRI run. The subsequent panels show equivalent plots for monkey Ba and monkey Mi. The bottom panel shows motion estimates from an agar phantom, with the columns representing different phase encoding directions (A–P: anterior-posterior; L–R: left-right). A linear trend of apparent posterior movement (cyan line) is present across all 15 fMRI runs, but is also present in the A-P phase encoding phantom acquisition (same as animal fMRI), but switches direction when the phase encoding is swapped to L-R, indicating that this trend is due to frequency drift in the phase encoding direction, rather than animal motion. True animal motion was minimal across all runs.

chamber to minimize head motion during awake marmoset fMRI at ultra-high field. By integrating the coil elements into the fixation device, the animal could be quickly head fixed (with a cage to scanning start time of less than 10 min), thereby minimizing stress to the animal. The integrated coil design also ensures consistent coil-to-brain referencing, with the radiofrequency coil always in the same position with respect to the fixation pins (and thus the brain). This rigid design minimizes head motion, as demonstrated here through 15 consecutive fMRI runs across three different marmosets (Fig. 5); consequently, a minimum amount of data (if any) needs to be discarded due to animal motion with this design (no data was discarded here). In contrast to previous designs for awake marmoset imaging (Papoti et al., 2013), our design is completely open above the skull (see Figs. 1 and 4) leaving room for electrode or lens placement (with 3-cm of head room available within a 12-cm-diameter transmit coil); the head chamber design used here was originally created to allow for linear electrode array placement (Johnston et al., 2018, 2019) and is compatible with a commercially available marmoset stereotactic recording chair (Neuronitek, London, Ontario, Canada). Accordingly, this design is appropriate for researchers interested in multimodal neuroimaging, both within the MRI community and across restraint modalities (i.e., upright chair fixation).

With multimodal imaging in mind, our design allows for stereotactic imaging by way of either: 1) stereotactic implantation of the chamber or 2) adjustment to the stereotactic position by modifying the pin inserts (Fig. 10) after implantation (i.e., by measuring head rotation through imaging and creating the opposite rotation through the pin inserts). Stereotactic imaging allows for ready identification of electrode recording targets, for example, based on fMRI patterns of activity – this localization can be aided by a chamber grid insert (Fig. 10C and D) filled with a high MR contrast liquid (e.g., betadine). If longer neuroimaging sequences are required (e.g., very high resolution anatomical imaging), or imaging prior to chair acclimatization, we have also included an

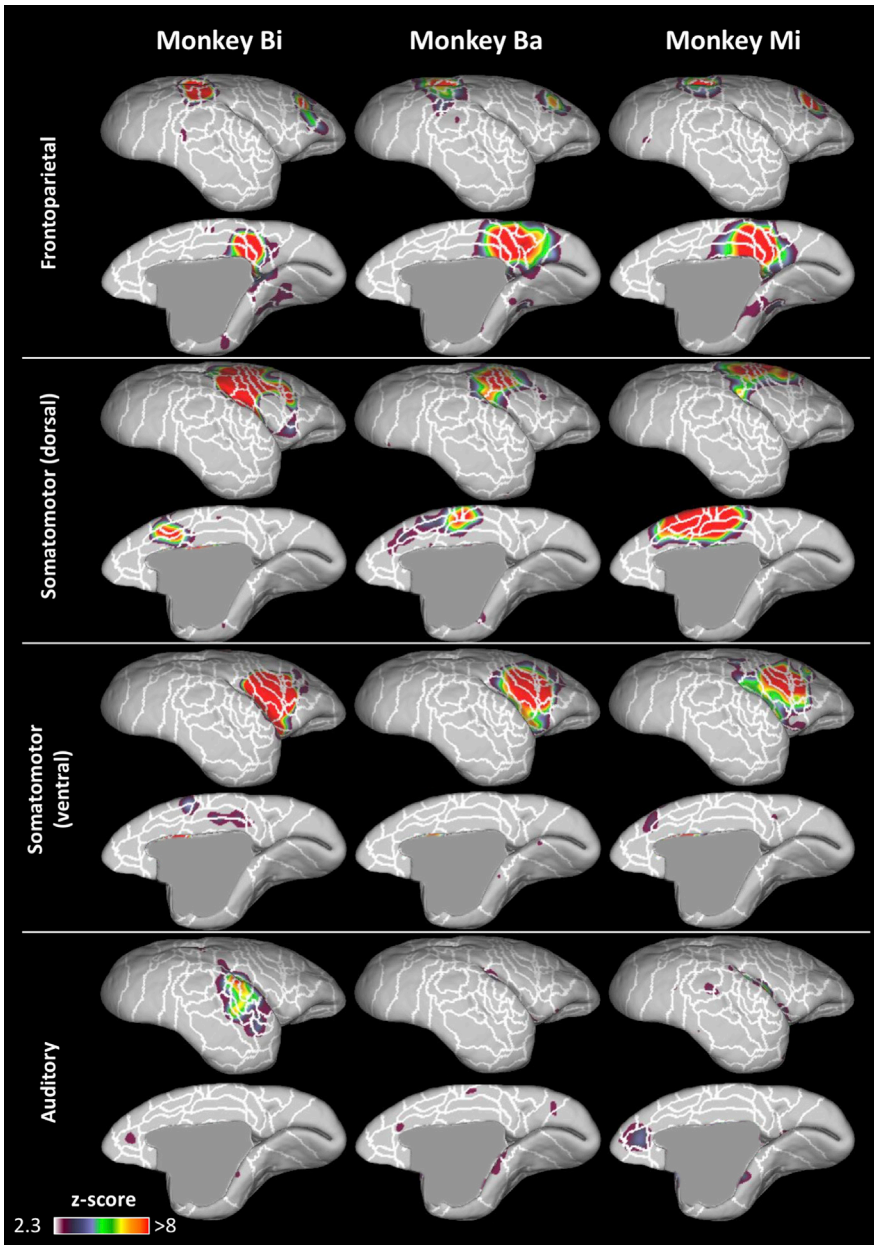

Fig. 6. Resting state networks derived from an ICA analysis conducted in each animal. Four of the eight networks (other four in Fig. 7) are shown as thresholded z-score maps on the NIH atlas surface (Liu et al., 2018). Right hemisphere only is shown due to space constraints (top, lateral; bottom, medial view), but left hemisphere is shown in volumetric maps (Fig. 8). Each monkey is shown as a column and separate networks are shown as rows. White lines show cytoarchitectonic borders for reference (Liu et al., 2018).

adjustable marmoset-specific anesthesia mask (Fig. 1). Finally, our design accommodates an MR-compatible camera and a liquid reward tube for awake task-based fMRI (e.g., saccadic eye movement tasks). This design is less ideal for auditory studies, as the coil former and elements occlude access to the ears. Because our designs are openly available, however, the CAD files can be fine-tuned for the specific research question at hand.

To evaluate the quality of the 5-channel receive coil design, geometric decoupling (S12), preamplifier decoupling, and active detuning were measured. The geometric decoupling between elements (mean = −18 dB, maximum = −12 dB), preamplifier decoupling (added a further 10–13 dB of isolation), and active detuning (mean isolation = −32 dB) were all found to be within a respectable range, especially given the large coil size requisite for the open chamber design (see Fig. 2). Spatial SNR of the individual channels differed by 23%, indicating similar sensitivity between coil elements. The coil design allowed for two-fold acceleration of functional images and yielded high quality resting state maps across 3 different marmosets. The quality of this data is demonstrated both in the motion estimates (see Fig. 5; most of which was due to frequency drift, rather than animal motion) and through the analysis of the fMRI data (via ICA). From the ICA analysis, we were able to reliably extract 8 resting state networks from a relatively limited amount of resting state data (Monkey Bi: 90 min, Monkey Ba: 60 min, Monkey Mi: 75 min).

As an index of quality, the awake resting state network maps shown here are comparable to those previously shown in group averages (Belcher et al., 2013) – we show reliable networks from each individual animal. Belcher et al. (2013) demonstrated high-quality resting state network maps in awake marmosets, but these data were derived from six different marmosets that were imaged at 80 min each (i.e., 8 h of total acquisition) – as little as 60 min (Monkey Ba) was required here to extract eight resting state networks from a single animal. Overall, our results are mostly consistent with the group ICA maps shown by Belcher et al. (2013). We showed eight consistent networks across the three animals: including frontoparietal, somatomotor (dorsal), somatomotor (ventral), auditory/thalamic, basal ganglia, primary visual, high-order visual, and

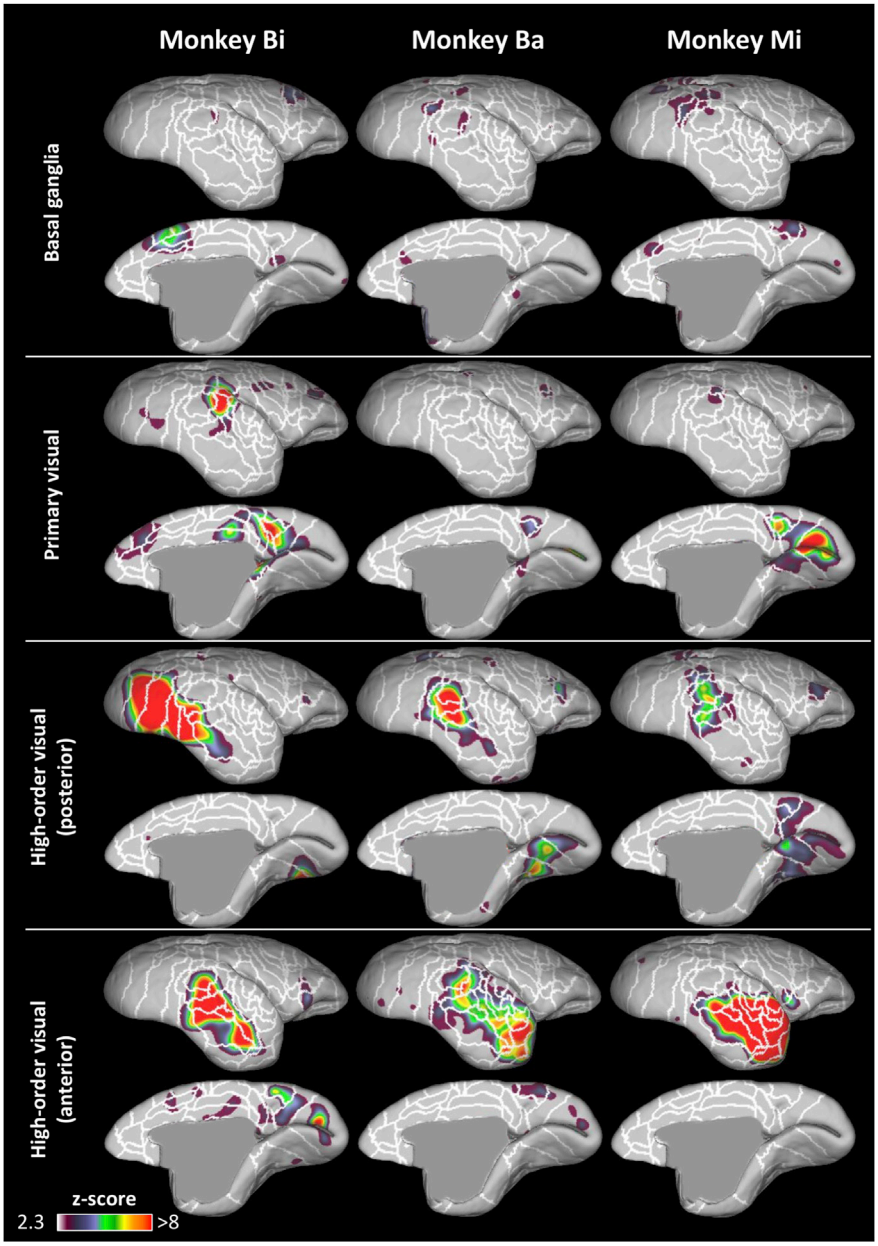

Fig. 7. Resting state networks derived from an ICA analysis conducted in each animal. Four of the eight networks (first four in Fig. 5) are shown as thresholded z-score maps on the NIH atlas surface (Liu et al., 2018). Right hemisphere only is shown due to space constraints (top, lateral; bottom, medial view), but left hemisphere is shown in volumetric maps (Fig. 9). Each monkey is shown as a column and separate networks are shown as rows. White lines show cytoarchitectonic borders for reference (Liu et al., 2018).

high-order visual (anterior) networks. When compared to Belcher et al. (2013), we did not show orbitofrontal, cerebellar (likely due to lack of coverage), or frontal pole networks; these networks, however, were among the least reproducible (and accounted for the least variance in the ICA analysis) in the Belcher et al. (2013) study, suggesting that these networks have relatively weak connectivity. Our results also compare well to group ICA resting state network maps derived from four anesthetized marmosets (Ghahremani et al., 2017).

A caveat of using of skull-attached chambers is that they are generally accompanied by magnetic susceptibility and inhomogeneity (via magnetic properties of the material/adhesive and surgical displacement of the skin, fat, and muscle). Although this was indeed the case here, we were able to circumvent the majority of the signal loss by filling the chamber with a water-based lubricant gel (see Fig. 4 for comparison with and without gel). This was inspired by Adamczak et al. (2010) wherein the authors molded agarose around the heads of mice for ultra-high field fMRI and saw a significant improvement in image quality by drastically improving homogeneity and thus decreasing geometric distortion. The same held true in the present study, with the magnitude of temporal SNR in frontal cortex dependent on the application of gel in the chamber, and also liberal application above the brow ridge (see Fig. 4 for photograph).

In summary, the aim of this study was to develop practical hardware for head-fixed awake marmoset fMRI. To that end, we were able to reliably acquire high-quality fMRI data across three otherwise naïve marmosets after a relatively short training period of three weeks (following traning procedures of Silva et al., 2011). Motion was minimized with our hardware setup, with a maximum head translation of less than 100 μm over the course of 15 consecutive fMRI runs (15 min each) across three different marmosets. Reliable resting state networks were also extracted from each marmoset. Although not shown here, our design is amenable for multimodal neuroimaging via the open-chamber design (wherein electrodes or lenses can be implanted) as well as task-based fMRI, with camera and reward-tube attachments. We have made the CAD files (and engineering drawings; supplemental Fig. 1) of the hardware openly available, with the majority of the parts 3D-printable at a relatively low cost (https://web.gin.g-node.org/everling_lab_marmosets/awake_marmoset_fMRI_hardware).

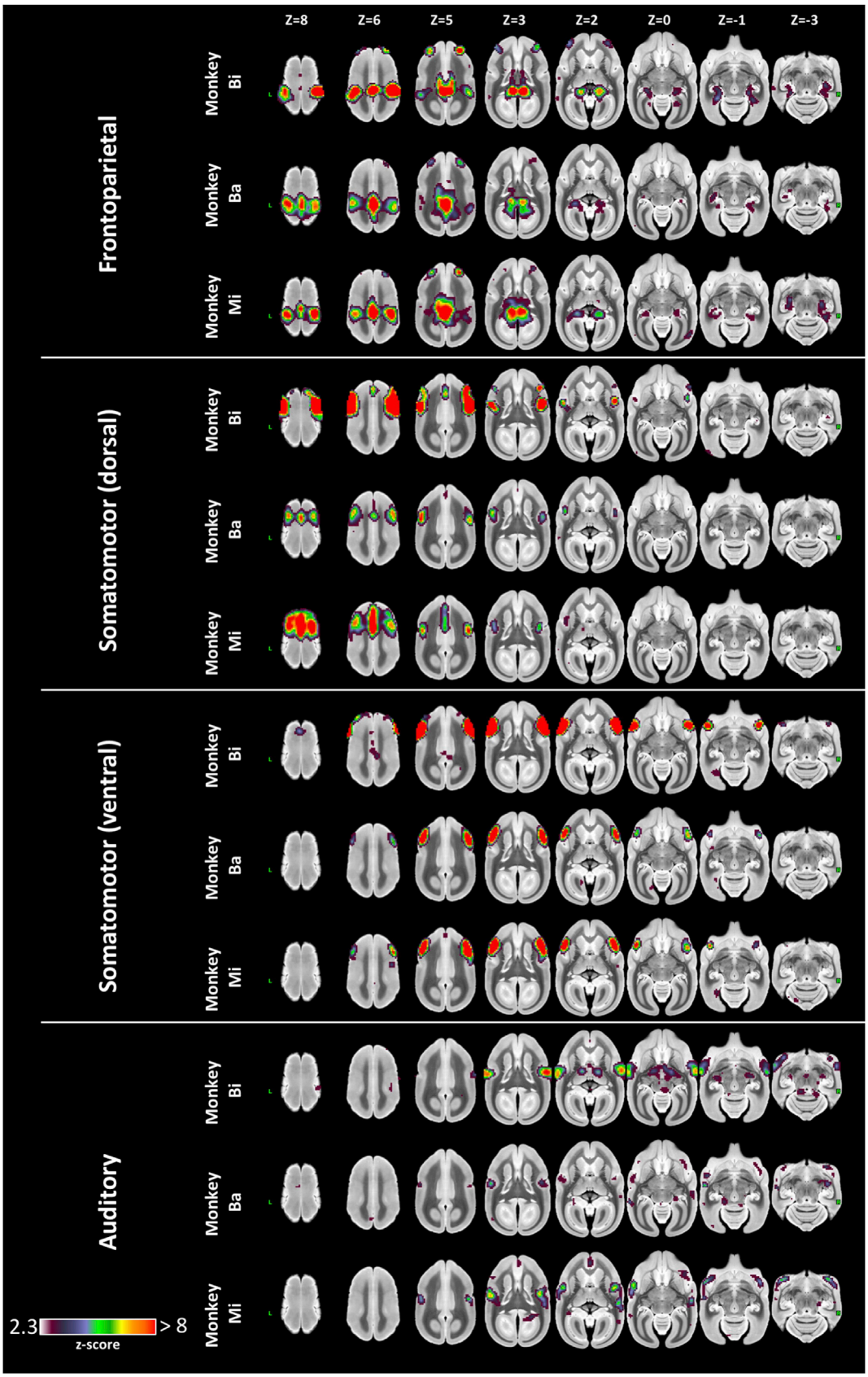

Fig. 8. Resting state networks derived from an ICA analysis conducted in each animal. Four of the eight networks (other four in Fig. 9) are shown as thresholded z-score maps on select slices of the NIH template brain (Liu et al., 2018). These are the same maps as Fig. 6, but shown volumetrically. Relative Z position of the slices is show at the top of the image and each monkey is shown as a row for each network.

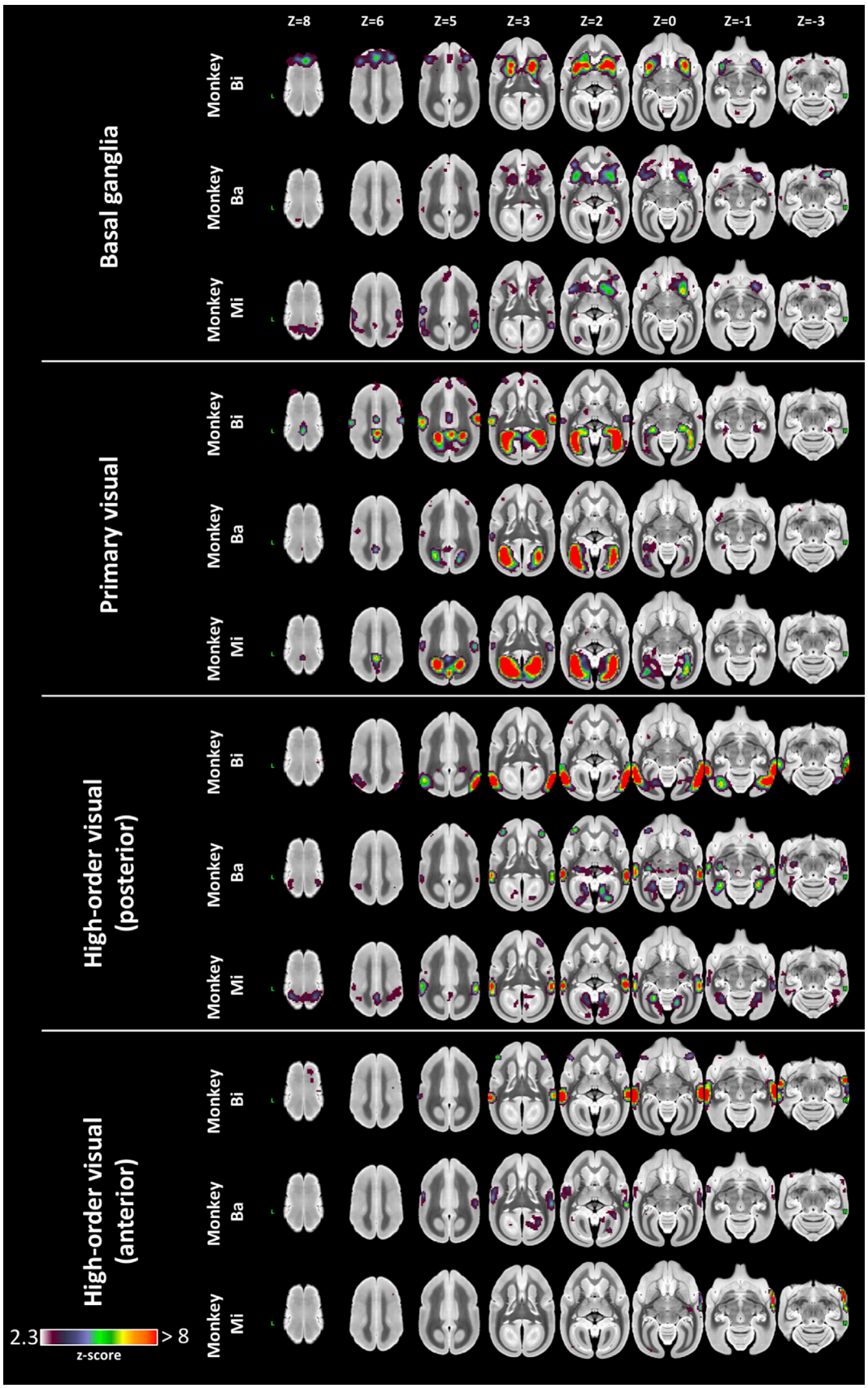

Fig. 9. Resting state networks derived from an ICA analysis conducted in each animal. Four of the eight networks (other four in Fig. 8) are shown as thresholded z-score maps on select slices of the NIH template brain (Liu et al., 2018). These are the same maps as Fig. 7, but shown volumetrically. Relative Z position of the slices is show at the top of the image and each monkey is shown as a row for each network.

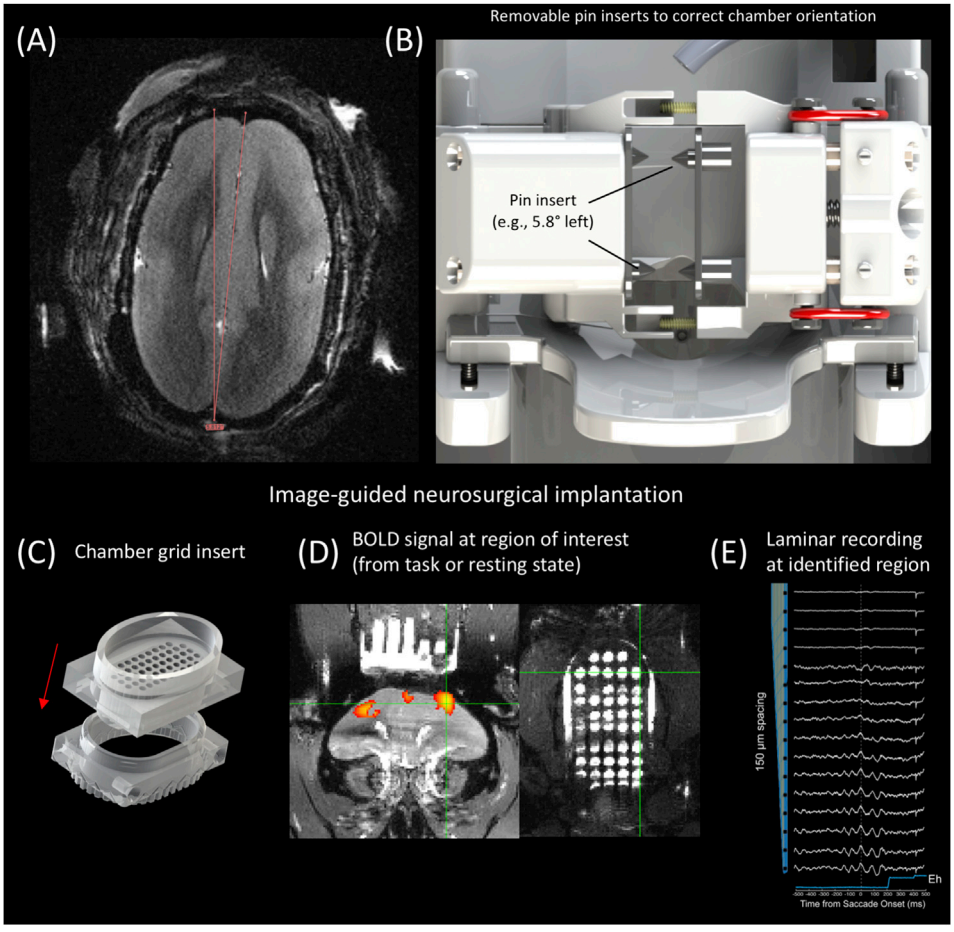

Fig. 10. Adjustment to stereotactic position based on T2-weighted image. Panel (A) shows estimation of needed rotation in the axial plane to put the marmoset's brain in stereotactic position (i.e., after the chamber is implanted). Panel (B) shows the fixation pin insert designs that can be used for each animal and allow for adjustment of the brain to stereotactic position. For example, the pins shown rotate the brain 5.8° to the left, aligning the brain in the axial plane. The removable pins allow for rotation in all three dimensions and can be interchanged for different marmosets (i.e., to compensate for head rotation of multiple animals without fabricating new coils or animal holders). Panel (C) shows a chamber grid insert that aides in locating neurosurgical implantation sites; when filled with a high contrast MR agent (e.g., betadine), these grid locations are easily visible in an anatomical image and can be referenced to fMRI signal change maps (panel D). These reference signals can then be used to locate the site for electrode implantation – panel (E) shows an example result of saccadic eye movement related activity from a laminar electrode implanted based on the blood-oxygen-level dependent (BOLD) signal localization in a marmoset.

Author notes

Support was provided by the Canadian Institutes of Health Research (FRN 148365) and the Canada First Research Excellence Fund to BrainsCAN. We wish to thank Miranda Bellyou and Lauren Schaeffer for animal preparation and care and Dr. Alex Li for scanning assistance.

Appendix A. Supplementary data

Supplementary data to this article can be found online at https://doi.org/10.1016/j.neuroimage.2019.03.023.

References

Adamczak, J.M., Farr, T.D., JU, Seehafer, Kalthoff, D., Hoehn, M., 2010. High field BOLD response to forepaw stimulation in the mouse. Neuroimage 51, 704–712.
Belcher, A.M., Yen, C.C.-C., Notardonato, L., Ross, T.J., Volkow, N.D., Yang, Y., Stein, E.A., Silva, A.C., Tomasi, D., 2016. Functional connectivity hubs and networks in the awake marmoset brain. Front. Integr. Neurosci. 10, 1–9.
Belcher, A.M., Yen, C.C., Stepp, H., Gu, H., Lu, H., Yang, Y., Silva, A.C., Stein, E.A., 2013. Large-scale brain networks in the awake, truly resting marmoset monkey. J. Neurosci. 33, 16796–16804.
Cox, R.W., 1996. AFNI: software for analysis and visualization of functional magnetic resonance neuroimages. Comput. Biomed. Res. 29, 162–173.
Ghahremani, M., Hutchison, R.M., Menon, R.S., Everling, S., 2017. Frontoparietal functional connectivity in the common marmoset. Cerebr. Cortex 27, 3890–3905.
Gilbert, K.M., Gati, J.S., Klassen, L.M., Zeman, P., Schaeffer, D.J., Everling, S., Menon, R.S., 2017. A geometrically adjustable receive array for imaging marmoset cohorts. Neuroimage 156.
Gilbert, K.M., Schaeffer, D.J., Gati, J.S., Klassen, L.M., Everling, S., Menon, R.S., 2019. Open-source hardware designs for MRI of mice, rats, and marmosets: integrated animal holders and radiofrequency coils. J. Neurosci. Methods 312, 65–72.
Goldman-Rakic, P.S., 1999. The physiological approach: functional architecture of working memory and disordered cognition in schizophrenia. Biol. Psychiatry 46, 650–661.
Griffanti, L., Douaud, G., Bijsterbosch, J., Evangelisti, S., Alfaro-Almagro, F., Glasser, M.F., Duff, E.P., Fitzgibbon, S., Westphal, R., Carone, D., Beckmann, C.F., Smith, S.M., 2017. Hand classification of fMRI ICA noise components. Neuroimage 154, 188–205.
Hirano, Y., Yen, C.C., Liu, J.V., Mackel, J.B., Merkle, H., Nascimento, G.C., Stefanovic, B., Silva, A.C., 2018. Investigation of the BOLD and CBV fMRI responses to somatosensory stimulation in awake marmosets (Callithrix jacchus). NMR Biomed. 31, 1–11.
Hung, C.-C., Yen, C.C., Ciuchta, J.L., Papoti, D., Bock, N.A., Leopold, D.A., Silva, A.C., 2015a. Functional mapping of face-selective regions in the extrastriate visual cortex of the marmoset. J. Neurosci. 35, 1160–1172.
Hung, C.C., Yen, C.C., Ciuchta, J.L., Papoti, D., Bock, N.A., Leopold, D.A., Silva, A.C., 2015b. Functional MRI of visual responses in the awake, behaving marmoset. Neuroimage 120, 1–11.
Hutchison, R.M., Hutchison, M., Manning, K.Y., Menon, R.S., Everling, S., 2014. Isoflurane induces dose-dependent alterations in the cortical connectivity profiles and dynamic properties of the brain's functional architecture. Hum. Brain Mapp. 35, 5754–5775.
Johnston, K.D., Barker, K., Schaeffer, L., Schaeffer, D., Everling, S., 2018. Methods for chair restraint and training of the common marmoset on oculomotor tasks. J. Neurophysiol. 119.
Johnston, K., Ma, L., Schaeffer, L., Everling, S., 2019. Alpha oscillations modulate preparatory activity in marmoset area 8Ad. J. Neurosci. 39, 1855–1866.
Keil, B., Alagappan, V., Mareyam, A., McNab, J.A., Fujimoto, K., Tountcheva, V., Triantafyllou, C., Dilks, D.D., Kanwisher, N., Lin, W., Grant, P.E., Wald, L.L., 2011. Size-optimized 32-channel brain arrays for 3 T pediatric imaging. Magn. Reson. Med. 66, 1777–1787.
Li, X., Morgan, P.S., Ashburner, J., Smith, J., Rorden, C., 2016. The first step for neuroimaging data analysis: DICOM to NIfTI conversion. J. Neurosci. Methods 264, 47–56.
Liu, C., Ye, F.Q., Yen, C.C.C., Newman, J.D., Glen, D., Leopold, D.A., Silva, A.C., 2018. A digital 3D atlas of the marmoset brain based on multi-modal MRI. Neuroimage 169, 106–116.
Liu, J.V., Hirano, Y., Nascimento, G.C., Stefanovic, B., Leopold, D.A., Silva, A.C., 2013. FMRI in the awake marmoset: somatosensory-evoked responses, functional connectivity, and comparison with propofol anesthesia. Neuroimage 78, 186–195.
Majka, P., Chaplin, T.A., Yu, H.H., Tolpygo, A., Mitra, P.P., Wójcik, D.K., Rosa, M.G.P., 2016. Towards a comprehensive atlas of cortical connections in a primate brain: mapping tracer injection studies of the common marmoset into a reference digital template. J. Comp. Neurol. 524, 2161–2181.

Meyer, J.S., Brevard, M.E., Piper, B.J., Ali, S.F., Ferris, C.F., 2006. Neural effects of MDMA as determined by functional magnetic resonance imaging and magnetic resonance spectroscopy in awake marmoset monkeys. Ann. N. Y. Acad. Sci. 1074, 365–376.
Papoti, D., Yen, C.C.-C., Mackel, J.B., Merkle, H., Silva, A., 2014. Awake marmosets at 7T, 26, 1395–1402.
Papoti, D., Yen, C.C.C., Hung, C.C., Ciuchta, J., Leopold, D.A., Silva, A.C., 2017. Design and implementation of embedded 8-channel receive-only arrays for whole-brain MRI and fMRI of conscious awake marmosets. Magn. Reson. Med. 78, 387–398.
Papoti, D., Yen, C.C.C., Mackel, J.B., Merkle, H., Silva, A.C., 2013. An embedded four-channel receive-only RF coil array for fMRI experiments of the somatosensory pathway in conscious awake marmosets. NMR Biomed. 26, 1395–1402.
Peterson, J., Chaddock, R., Dalrymple, B., Van Sas, F., Gilbert, K.M., Klassen, L.M., Gati, J.S., Handler, W.B., Chronik, B.A., 2018. Development of a gradient and shim insert system for marmoset imaging at 9.4 T. Proceedings of the 26th Annual Meeting ISMRM, p. 4421 (Paris, France).
Preuss, T., 1995. Do rats have prefrontal cortex? The rose-woolsey-akert program reconsidered. J. Cogn. Neurosci. 7, 1–24.
Roemer, P.B., Edelstein, W.A., Hayes, C.E., Souza, S.P., Mueller, O., 1990. The NMR phased-array. Magn. Reson. Med. 16, 192–225.
Schaeffer, D.J., Gilbert, K.M., Ghahremani, M., Gati, J.S., Menon, R.S., Everling, S., 2019a. Intrinsic functional clustering of anterior cingulate cortex in the common marmoset. Neuroimage 186, 301–307.
Schaeffer, D.J., Gilbert, K.M., Gati, J.S., Menon, R.S., Everling, S., 2019b. Intrinsic functional boundaries of lateral frontal cortex in the common marmoset monkey. J. Neurosci. 39, 1020–1029.
Silva, A.C., 2017. Anatomical and functional neuroimaging in awake, behaving marmosets, 77, 373–389.
Silva, A.C., Liu, J.V., Hirano, Y., Leoni, R.F., Merkle, H., Mackel, J.B., Zhang, X.F., Nascimento, G.C., Stefanovic, B., 2011. Longitudinal functional magnetic resonance imaging in animal models. Methods Mol. Biol. 711, 281–302.
Smith, S.M., Jenkinson, M., Woolrich, M.W., Beckmann, C.F., Behrens, T.E.J., Johansen-Berg, H., Bannister, P.R., De Luca, M., Drobnjak, I., Flitney, D.E., Niazy, R.K., Saunders, J., Vickers, J., Zhang, Y., De Stefano, N., Brady, J.M., Matthews, P.M., 2004. Advances in functional and structural MR image analysis and implementation as FSL. Neuroimage 23, S208–S219.
Toarmino, C.R., Yen, C.C.C., Papoti, D., Bock, N.A., Leopold, D.A., Miller, C.T., Silva, A.C., 2017. Functional magnetic resonance imaging of auditory cortical fields in awake marmosets. Neuroimage 162, 86–92.
Walker, J., MacLean, J., Hatsopoulous, N.G., 2017. The marmoset as a model system for studying voluntary motor control. Dev. Neurobiol. 77, 273–285.
Yen, C.C.C., Cvetesic, N., Silva, A.C., 2018. Investigating the spatiotemporal characteristics of the deoxyhemoglobin-related and deoxyhemoglobin-unrelated functional hemodynamic response across cortical layers in awake marmosets. Neuroimage 164, 121–130.